

Regulation of interneuron excitability by gap junction coupling with principal cells

Pierre F Apostolides^{1,2} & Laurence O Trussell²

Electrical coupling of inhibitory interneurons can synchronize activity across multiple neurons, thereby enhancing the reliability of inhibition onto principal cell targets. It is unclear whether downstream activity in principal cells controls the excitability of such inhibitory networks. Using paired patch-clamp recordings, we show that excitatory projection neurons (fusiform cells) and inhibitory stellate interneurons of the dorsal cochlear nucleus form an electrically coupled network through gap junctions containing connexin36 (Cxc36, also called Gjd2). Remarkably, stellate cells were more strongly coupled to fusiform cells than to other stellate cells. This heterologous coupling was functionally asymmetric, biasing electrical transmission from the principal cell to the interneuron. Optogenetically activated populations of fusiform cells reliably enhanced interneuron excitability and generated GABAergic inhibition onto the postsynaptic targets of stellate cells, whereas deep afterhyperpolarizations following fusiform cell spike trains potently inhibited stellate cells over several hundred milliseconds. Thus, the excitability of an interneuron network is bidirectionally controlled by distinct epochs of activity in principal cells.

Cerebellum-like structures of vertebrates are thought to act as adaptive filters of ongoing sensory information, reducing the salience of predictable sensory input patterns^{1–3}. The principal efferent neurons of these circuits integrate two types of excitatory synapses: ‘instructive’ signals from a specific sensory modality and ‘predictive’ signals from other brain nuclei that convey the multisensory context in which the instructive signal occurred. Although these basic anatomical motifs are conserved across most cerebellum-like structures, the cellular mechanisms and local computations underlying the adaptive filtering of sensory information remain poorly understood¹.

The dorsal cochlear nucleus (DCN) is an auditory brainstem region that is thought to function as an adaptive filter to cancel predictable, self-generated sounds^{3,4}. Like other cerebellum-like structures, the DCN is divided into instructive and predictive pathways that converge on principal neurons^{1,3}, an anatomical layout suggesting that auditory information and multisensory information are processed by nonoverlapping circuits. The glutamatergic principal neurons (termed fusiform or pyramidal cells) integrate sound frequency information from tonotopically organized auditory nerve synapses with multisensory signals that are relayed by granule cell parallel fibers (Fig. 1a). The parallel fiber pathway also recruits two types of inhibitory interneurons in the molecular layer of the DCN: Purkinje-like cartwheel cells and superficial stellate cells that are analogous to the stellate and basket cells of the cerebellum⁴. Although fusiform cells receive convergent excitation from multisensory parallel fibers and the auditory nerve, the inhibitory stellate and cartwheel interneurons of the molecular layer receive only parallel fiber input. This suggests that although multisensory signals may filter auditory inputs by recruiting interneurons to modify fusiform cell spiking⁵, auditory nerve synapses do not directly control the activity of molecular-layer interneurons.

We find that the GABAergic stellate interneurons of the molecular layer are electrically coupled to the excitatory fusiform cells that integrate auditory and multisensory inputs. This newly identified circuit motif is surprising, as electrical coupling in the brain occurs primarily between inhibitory neurons of the same anatomical and functional class^{6,7}. These heterologous electrical synapses showed directional asymmetry, thereby favoring transmission from the auditory to the multisensory processing domains. Accordingly, the functional consequences of electrical coupling were such that stimulating auditory nerve synapses onto fusiform cells reliably depolarized stellate cells, and fusiform cell activity was sufficient to generate robust inhibition in the multisensory pathway. Our data substantially revise the connectivity map of the DCN and show that at the first synapses of the central auditory system, interneuron excitability is temporally controlled by the activity of projection neurons through electrical synapses.

RESULTS

Electrical coupling between interneurons and principal cells

We made whole-cell current-clamp recordings from pairs of fusiform and stellate cells in DCN-containing brain slices from 15- to 32-day-old wild-type mice. We identified neurons on the basis of morphological and electrophysiological criteria (Online Methods). In 92/203 attempted pairs (45%), hyperpolarizing one neuron (the ‘prejunctional’ cell) with an injection of negative current caused a simultaneous hyperpolarization in the other cell (the ‘postjunctional’ cell; Fig. 1b). The bidirectional translation of negative, subthreshold membrane potential deflections across two neurons is a hallmark of electrical coupling⁶.

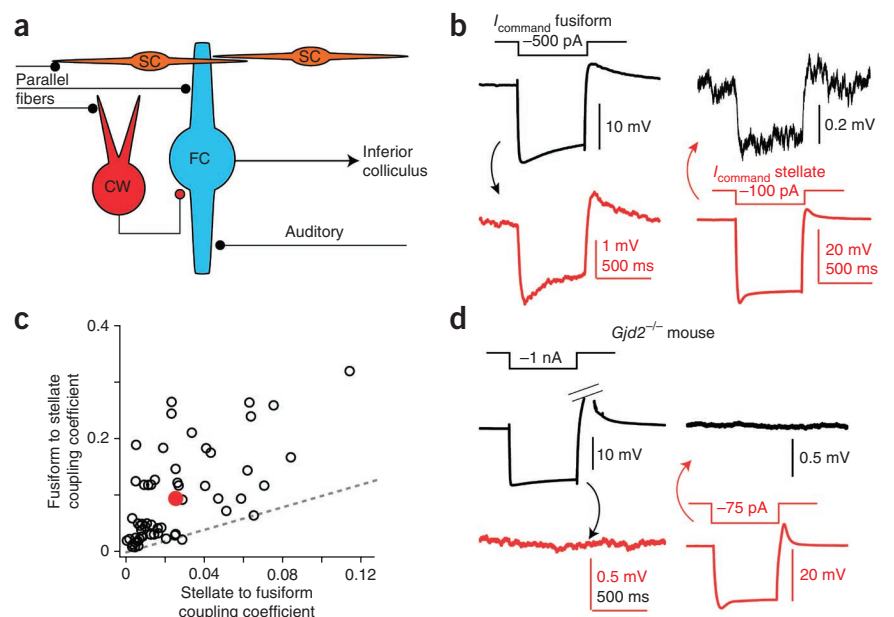
For 57 pairs in which we tested transmission bidirectionally, we calculated a coupling coefficient, which is defined as the ratio of the mean hyperpolarization during the last 50–100 ms of the current step

¹Neuroscience Graduate Program, Oregon Health and Science University, Portland, Oregon, USA. ²Vollum Institute and Oregon Hearing Research Center, Oregon Health and Science University, Portland, Oregon, USA. Correspondence should be addressed to L.O.T. (trussell@ohsu.edu).

Received 17 July; accepted 30 September; published online 3 November 2013; doi:10.1038/nn.3569

Figure 1 Asymmetric electrical coupling between DCN fusiform and stellate cells.

(a) Diagram of the DCN circuitry. The excitatory projection neurons of the DCN (fusiform cells (FC)) integrate excitatory auditory nerve and multisensory parallel fiber synapses⁴. Parallel fibers, but not auditory nerve fibers, impinge on two distinct types of inhibitory interneurons: cartwheel cells (CW) and superficial stellate cells (SC). (b) Example average traces from an electrically coupled fusiform and stellate pair. Injection of negative current into the fusiform cell (black trace) causes the expected hyperpolarization. This causes a smaller voltage deflection with a similar time course in the simultaneously recorded stellate cell (red trace; of note, the scale is different in the two traces). Similarly, hyperpolarizing the stellate cell causes a small voltage deflection in the fusiform cell. (c) Summary of the coupling coefficients for 57 pairs similar to that in b. The red point is the average \pm s.e.m. of the data set, and dashed gray line represents the unity line. Almost all pairs fall above the unity line, showing that the coupling coefficient is stronger in the fusiform to stellate direction compared to the opposite direction. (d) Example average traces from a typical paired recording in a DCN slice from a *Gjd2*^{-/-} mouse. The color coding is as in b. Out of 60 attempts, only 3 pairs were connected.



in postjunctional and prejunctional cells. Surprisingly, we found that coupling strength showed a strong directional preference such that the average coupling coefficient in the fusiform to stellate direction was 0.10 ± 0.01 (mean \pm s.e.m.) but was only 0.026 ± 0.003 in the stellate to fusiform direction (Fig. 1c,d). Although electrical coupling is stronger in neonates in some brain regions^{8,9}, coupling remained robust in DCN slices from mice at 7–9 weeks of age (connection probability, 10/16, or 62.5%). For pairs recorded in these more mature animals, the average fusiform to stellate cell coupling coefficient was 0.13 ± 0.04 ($n = 8$ pairs tested in this direction), whereas the stellate to fusiform coupling coefficient was 0.026 ± 0.005 ($n = 5$ pairs tested). These results show that the excitatory projection neurons of the DCN form strong, developmentally persistent electrical synapses with local inhibitory interneurons. Furthermore, the directional asymmetry is such that the coupling from fusiform to stellate cells is nearly four-fold stronger than that in the opposite direction. Using a previously described approach¹⁰, we also calculated the junctional conductances for each direction and found an average fusiform to stellate cell conductance of 0.41 ± 0.04 nS (mean \pm s.e.m.) and a stellate to fusiform conductance of 0.98 ± 0.11 nS ($n = 57$ pairs; Online Methods).

Electrical coupling requires connexin36-containing gap junctions

Similarly to that in other brain regions⁶, electrical coupling was significantly compromised in DCN slices from mutant mice lacking the neuronal gap junction channel connexin36 (*Gjd2*^{-/-} mice; Fig. 1d). Only 3/60 attempted pairs were coupled in these mice ($\chi^2 = 30.9$, $P < 0.0001$ compared to wild-type mice). The average fusiform to stellate coupling coefficient of the remaining coupled pairs was 0.024 ± 0.012 ($n = 3$), whereas the coupling was 0.003 ± 0.001 in the opposite direction ($n = 2$). Furthermore, electrical coupling in wild-type mice was blocked by a 15- to 30-min bath application of the gap junction blocker meclofenamic acid (MFA; Supplementary Fig. 1). Together these data show that electrotonic coupling between fusiform and stellate cells reflects electrical synapses between two different cell types and that this coupling requires connexin36.

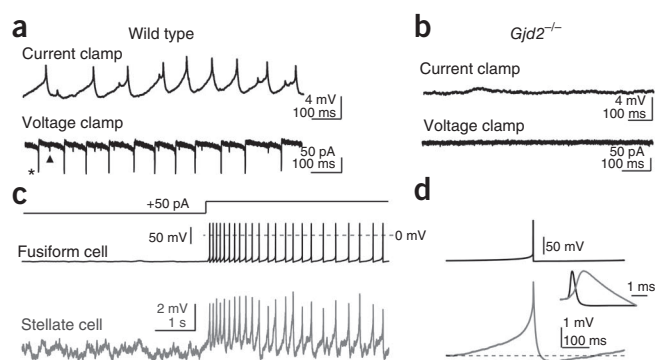
These results are surprising, as electrical coupling in the brain is typically observed between neurons of the same class^{7,11}. We therefore

asked how coupling between fusiform and stellate cells contrasts with the efficacy of electrical transmission between the same cell types. We indeed found that electrical coupling occurred between stellate cells (9/42 of attempted pairs; Supplementary Fig. 2a), as predicted from an anatomical study in the DCN¹² and by homology to cerebellar stellate cells¹³ (Supplementary Fig. 2b). However, the homologous coupling between stellate cells (0.024 ± 0.005 , average of both directions) was much weaker than the fusiform to stellate cell coupling. Notably, we also found electrical coupling in the majority of attempted fusiform cell pairs (20/28; Supplementary Fig. 3), although this coupling was again weak (0.014 ± 0.001). By contrast, we found no evidence for electrical coupling between fusiform cells and another major molecular layer interneuron, the cartwheel cell (0/27 connected pairs; data not shown). This result highlights a strong specificity of electrical coupling in the DCN, as cartwheel cells make potent inhibitory synapses onto fusiform cells and overlap extensively in their dendritic fields⁴. Together our data reveal a broad, cell type-specific network of gap junction-mediated communication between excitatory and inhibitory neurons in the DCN molecular layer and show that electrical transmission is biased largely toward heterologous coupling in the fusiform to stellate cell direction.

Propagation of fusiform cell spikes into stellate cells

Previous studies have shown that fusiform cells fire spontaneously *in vitro*^{5,14} and *in vivo*¹⁵. The strong coupling between fusiform and stellate cells suggests that these spikes could modulate the membrane potential of electrically coupled stellate cells. Accordingly, we observed spontaneous, subthreshold spikelets in the majority of current-clamp recordings from single stellate cells (44/65, or 67%; Fig. 2a). In voltage-clamp recordings, the spikelets were clearly biphasic, with a fast inward current that was followed by a slower, smaller outward current (Fig. 2a). These events were due to electrical coupling, as they occurred in the presence of glutamate, GABA_A and glycine receptor antagonists and were absent in recordings from *Gjd2*^{-/-} mice (Fig. 2b). Furthermore, paired recordings revealed that action potentials in prejunctional fusiform cells evoked spikelets in the postjunctional

Figure 2 Fusiform cells generate spikelets in electrically coupled stellate cells. **(a)** Spontaneous spikelet activity in a single stellate cell recorded in current and voltage clamp (upper and lower traces, respectively). Recordings were performed in the presence of glutamate, glycine and GABA_A receptor blockers. Spikelet events with two distinct amplitudes are apparent (examples are indicated with the asterisk and triangle), suggesting that at least two prejunctional fusiform cells with different coupling coefficients are coupled to the same stellate cell. **(b)** As in **a** but performed in a *Gjd2*^{-/-} mouse. No spikelets were detected in these knockout mice (0/77 cells tested; $\chi^2_1 = 72.4$, $P < 0.0001$ compared to wild-type mice). Traces were recorded in the presence of synaptic blockers. **(c)** Paired recording from electrically coupled fusiform and stellate cells (upper and lower traces, respectively). The fusiform cell was driven to spike by current injection. Of note, there was immediate onset, uniform amplitude and lack of transmission failures of spikelets in the stellate cell. **(d)** Averages (acquisition triggered by detection of the prejunctional spike) from the same pair as that shown in **c**. Only spikes that occurred more than 300 ms apart were included in the average to highlight the time course of the depolarizing and hyperpolarizing phases of the spikelet waveform. The inset shows the spikelet rising phase on a fast time base normalized to the peak of the prejunctional spike, highlighting that spikelets rise before the downswing of the action potential of the fusiform cell.



stellate cell (Fig. 2c). We also determined the spikelet amplitude and latency by generating a fusiform cell spike-triggered average of stellate cell spikelets from our paired recordings (Fig. 2d). Spikelets had an average positive peak amplitude of 0.9 ± 0.2 mV (mean \pm s.e.m.) and a mean latency from the peak of the prejunctional spike to that of the postjunctional spikelet of 837 ± 72 μ s (mean \pm s.e.m.; $n = 11$ pairs). Furthermore, we never observed spikelet transmission failures, indicating that fusiform cell spikes reliably propagate to stellate cells.

Stellate cell somata lie primarily near the DCN ependyma¹², suggesting that electrical synapses are located in fusiform cell apical dendrites. In a subset of our paired recordings, we investigated the location of putative contacts by first visualizing the morphology of fusiform cells with a fluorophore (Alexa488 or Alexa594) in the pipette internal solution and then selectively targeting stellate cells located near the apical dendrites of the fusiform cell. This method significantly increased the probability of finding an electrically coupled pair from 36% without *a priori* visualization of fusiform cell morphology (41/113) to 57% when we targeted stellate cells near fusiform

cell dendrites (51/90; $\chi^2_1 = 7.6$, $P = 0.006$). We further characterized the anatomical organization of electrical coupling by imaging connected pairs using two-photon microscopy. We filled fusiform and stellate cells with Alexa488 (90 μ M) and Alexa594 (20–30 μ M) dyes, respectively, and determined the relative organization of stellate and fusiform cell processes (Fig. 3a). We consistently ($n = 11$ electrically coupled pairs) observed that stellate cell processes were restricted primarily (though not exclusively) to the distal region of fusiform cell apical dendrites, which is in agreement with previous work¹². Moreover, the dendritic arbors of the two cell types could be in close apposition (Fig. 3a), suggesting putative points of contact.

Previous studies have suggested that action potentials in fusiform cells back propagate into the apical dendrites^{16,17}. The slower waveform of the spikelet as compared to the fusiform cell action potential suggests that the latter may be filtered as it propagates to the stellate cell, although the lack of transmission failures argues that fusiform cell spikes nevertheless reliably propagate through the apical dendrites (Fig. 2c,d). In agreement with this interpretation, two-photon Ca^{2+}

Figure 3 Fusiform cell action potentials propagate into the distal apical dendrites. **(a)** Top, two-photon maximum-intensity z stack from the example pair shown in Figure 1b. The stellate and fusiform cells are filled with Alexa594 (red) and Alexa488 (green) dyes, respectively. The dashed white line represents the approximate ependymal border of the DCN. Stellate cell processes do not extend into the cell body layer, whereas fusiform cell processes span the entire length of the DCN. Bottom left, a maximal intensity z stack at higher magnification from the same pair. Bottom right, high-magnification single optical section of the area denoted by the white arrow in the image to the left showing a high degree of overlap between the stellate and fusiform cell processes (white dots). **(b)** Right, maximum intensity two-photon z stack from a representative fusiform cell showing the line scan locations during the Ca^{2+} imaging experiment (red arrowheads labeled 1–5). Left, example sweeps of action potential-evoked Fluo-5F Ca^{2+} transients (five spikes, 50 Hz) recorded at the corresponding dendritic locations marked in the z stack (shown on the left). Each trace is an average of 20–25 trials. **(c)** Absolute $\Delta G/R$ values plotted as a function of approximate distance from the soma. The response amplitudes are relatively constant along the dendrite. Each data point represents the mean value \pm s.e.m. from three to six individual cells.

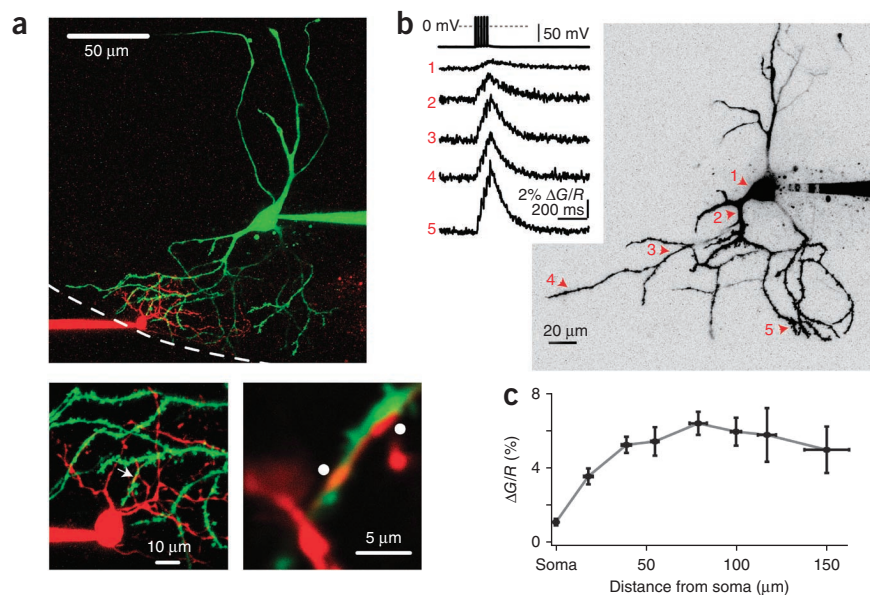
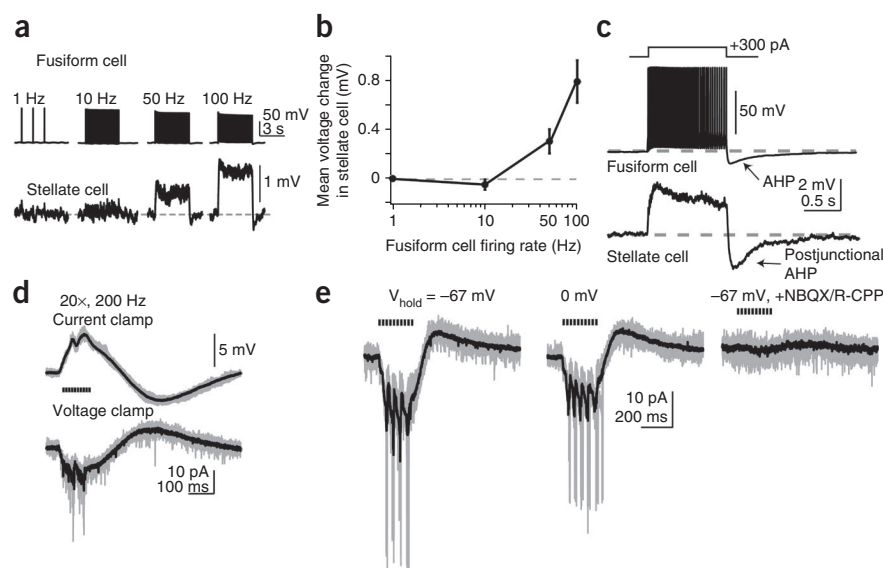


Figure 4 Control of the stellate cell membrane potential by fusiform cells and auditory nerve activity. **(a)** Upper traces, fusiform cell spikes evoked at different frequencies (single trials). Lower traces, averages of 50–54 trials in an electrically coupled stellate cell. **(b)** Summary data ($n = 9$) showing the stellate cell mean voltage change \pm s.e.m. from baseline plotted against the fusiform cell spike frequency. **(c)** Current injection in a fusiform cell triggered high-frequency firing followed by post-train AHP after stimulus offset (upper trace). A simultaneously recorded, postjunctional stellate cell (lower trace) was transiently depolarized above baseline during fusiform cell spiking and hyperpolarized by the AHP after stimulus termination. The top trace shows a single trial, and the bottom trace shows an average of eight sweeps. **(d)** Activation of the auditory nerve elicits biphasic signals in stellate cells. A stimulating electrode was placed in the ventral cochlear nucleus (VCN) $>600 \mu\text{m}$ from the recorded cell in the DCN.



Shown is a representative stellate cell recorded in current or voltage clamp (upper and lower traces, respectively) during stimulation of the VCN (20 shocks at 5-ms intervals). In current clamp, a negative bias current (-30 pA) was injected to prevent spike generation. **(e)** VCN stimuli (ten shocks at 50 Hz) were delivered while the cell was clamped at -67 or 0 mV . Little difference was seen in the response amplitudes at the two potentials. Right trace, $10 \mu\text{M}$ NBQX and $5 \mu\text{M}$ R-CPP ($+ \text{NBQX/R-CPP}$) eliminated the response, as was expected for glutamatergic transmission from the auditory nerve. For **d** and **e**, the gray traces show results from five consecutive trials, and black traces are the averages of 12–31 trials. Recordings were made in the presence of $1 \mu\text{M}$ strychnine and $10 \mu\text{M}$ SR95531. Stimulus artifacts were blanked.

imaging of fusiform cells loaded with Alexa594 and the Ca^{2+} indicator Fluo-5F ($150\text{--}200 \mu\text{M}$) revealed that the action potentials invaded the entire apical arbor (Fig. 3b,c). As expected from the back propagation of action potentials, the absolute amplitude of the action potential-evoked $\Delta\text{G/R}$ signal (Online Methods) did not attenuate as a function of approximate distance from the soma but instead remained constant throughout the distal processes ($n = 6$ cells; Fig. 3c). Together these data argue that spikelets in stellate cells originate as action potentials that have propagated through the apical dendritic arbor of the fusiform cell. Moreover, the obvious size difference between fusiform and stellate cells suggests that impedance mismatch contributes to the coupling asymmetry observed (Fig. 1). Accordingly, we found that the input resistances for the two cells differed by over tenfold (fusiform cells, $87 \pm 37 \text{ M}\Omega$ (mean \pm s.e.m.);¹⁸ stellate cells, $996 \pm 139 \text{ M}\Omega$ ($n = 29$), found here).

Frequency dependence of transmission

Previous studies have suggested that spikelets may exert a predominantly inhibitory effect on the postjunctional cell, as the low-pass filter properties of gap junction channels allow preferential passage of the spike afterhyperpolarization (AHP) as compared to the faster depolarizing Na^+ upstroke^{19,20}. Indeed, our paired recordings (Fig. 2d) show that fusiform to stellate cell spikelets are biphasic, with a prominent negative-going phase. However, other studies have indicated that the shape of the postjunctional spikelets depends on the firing rate of the prejunctional cell and that the hyperpolarizing trough disappears at frequencies $>50 \text{ Hz}$ (ref. 21). We therefore asked whether the prejunctional spike frequency determines whether fusiform cells exert a net depolarizing or a net hyperpolarizing effect on stellate cells. We evoked spikes in fusiform cells at different frequencies and measured the mean change in membrane potential of the stellate cells to which they were coupled (Fig. 4a,b). We hyperpolarized the stellate cells with a constant bias current to prevent action potentials. Fusiform cell spikes evoked at 1 and 10 Hz had no effect on the mean membrane

potential in the stellate cells (1 Hz, $0.005 \pm 0.009 \text{ mV}$; 10 Hz, $-0.04 \pm 0.04 \text{ mV}$; $n = 9$ pairs). Thus, during low-frequency activity similar to that observed *in vivo* during periods of quiescence, fusiform cell activity does not cause the membrane potential of the stellate cell to deviate appreciably from baseline. Conversely, high-frequency fusiform cell activity (50 and 100 Hz) had a net excitatory effect, causing mean voltage changes of $+0.3 \text{ mV} \pm 0.1 \text{ mV}$ and $+0.8 \pm 0.2 \text{ mV}$, respectively. Given that fusiform cells can fire at $>200 \text{ Hz}$ during sound-evoked activity *in vivo*^{15,22}, these data indicate that physiological spike rates in single fusiform cells depolarize the membrane potential of electrically coupled interneurons in a frequency-dependent manner.

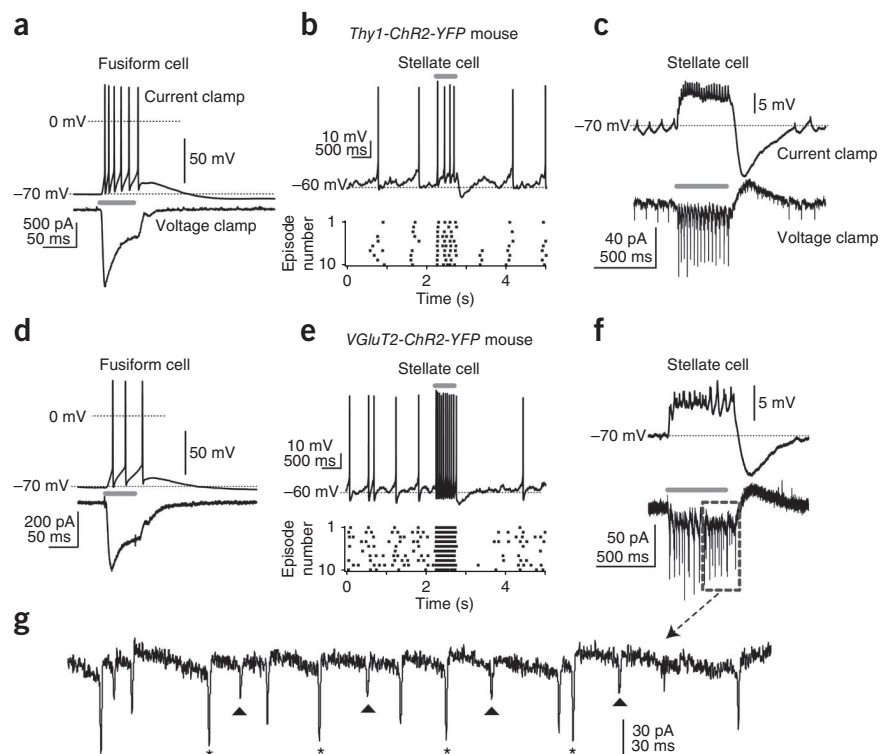
After a spike train in fusiform cells, a post-train AHP was invariably apparent. For trains elicited by square-pulse current injection ($0.3\text{--}1 \text{ nA}$, $0.4\text{--}1 \text{ s}$), the negative peak of the AHP was $-11.3 \pm 1.0 \text{ mV}$ below rest, with a half width of $406 \pm 58 \text{ ms}$ (mean \pm s.e.m.; $n = 8$ fusiform cells; Fig. 4c). Intracellular recordings from fusiform cells driven by acoustic stimuli *in vivo* show that this AHP occurs after sound termination^{23,24}, indicating that the AHP is not an artifact of direct current injection through the recording pipette. Paired recordings revealed that the post-train AHP in fusiform cells reliably invaded the stellate cells ($n = 7$ pairs; Fig. 4c). Interestingly, the absolute peak amplitude of the postjunctional AHP in stellate cells was $92 \pm 8\%$ (mean \pm s.e.m.) that of the steady-state depolarizing phase, suggesting that the positive- and negative-going phases of fusiform cell activity may be of comparable importance to stellate cells.

Auditory nerve activity is transmitted to stellate cells

Auditory nerve fibers contact the basal dendrites of fusiform cells but do not extend into the DCN molecular layer²⁵. However, single fusiform cells can control the membrane potential of electrically coupled stellate cells (Fig. 4a–c), suggesting that acoustic information from the auditory nerve may nevertheless reach stellate cells through electrical synapses. We explicitly tested the possibility that stellate cells sense activity in the auditory pathway by recording from single stellate cells

Figure 5 Optogenetic activation of fusiform cells depolarizes stellate cells. **(a)** In a *Thy1-ChR2-YFP* fusiform cell, light stimuli (50 ms; gray bar) generate spikes in current clamp (upper traces) and photocurrents in voltage clamp (lower traces). The top trace shows a single trial, and the lower trace shows an average of nine trials. **(b)** Top, current-clamp recording from a stellate cell in a *Thy1-ChR2-YFP* mouse (zero bias current). A 500-ms light stimulus (gray bar) causes an immediate increase in spike frequency. Bottom, raster plot of ten trials highlighting the increase in spike rate after optogenetic stimulation of fusiform cells. Similar results were obtained in 18/19 stellate cells.

(c) A stellate cell in a *Thy1-ChR2-YFP* mouse (a different cell from that in **b**). Top trace, current-clamp recording, with a -25 pA bias current injected to hyperpolarize the cell and prevent spike generation. A light flash (400 ms) causes spikelets riding atop a steady-state depolarization followed by an AHP at light offset. Of note, there is similarity to the traces in **Figure 4c**. Lower trace, the same stimulus delivered when the cell is voltage clamped at -70 mV causes a barrage of fast inward spikelets followed by a slow outward current after stimulus offset. Traces show single trials. **(d)** A fusiform cell in a *VGLUT2-ChR2-YFP* mouse. As in the cell in a *Thy1-ChR2-YFP* mouse shown in **a**, light (50 ms) drives spikes and induces photocurrents. The current-clamp trace is a single sweep, and the voltage-clamp trace is an average of ten trials. **(e)** Current-clamp recording from a stellate cell in the *VGLUT2-ChR2-YFP* mouse. The experiment and layout are as in **b**. **(f)** A stellate cell in a *VGLUT2-ChR2-YFP* mouse showing that light stimuli cause depolarizations and inward currents, as in the *Thy1-ChR2-YFP* mouse. **(g)** Enlargement of the area denoted by the gray dashed rectangle in **f**. Spikelets with distinct amplitudes (denoted by triangles and asterisks) are present, suggesting coupling to at least two fusiform cells with different coupling coefficients.



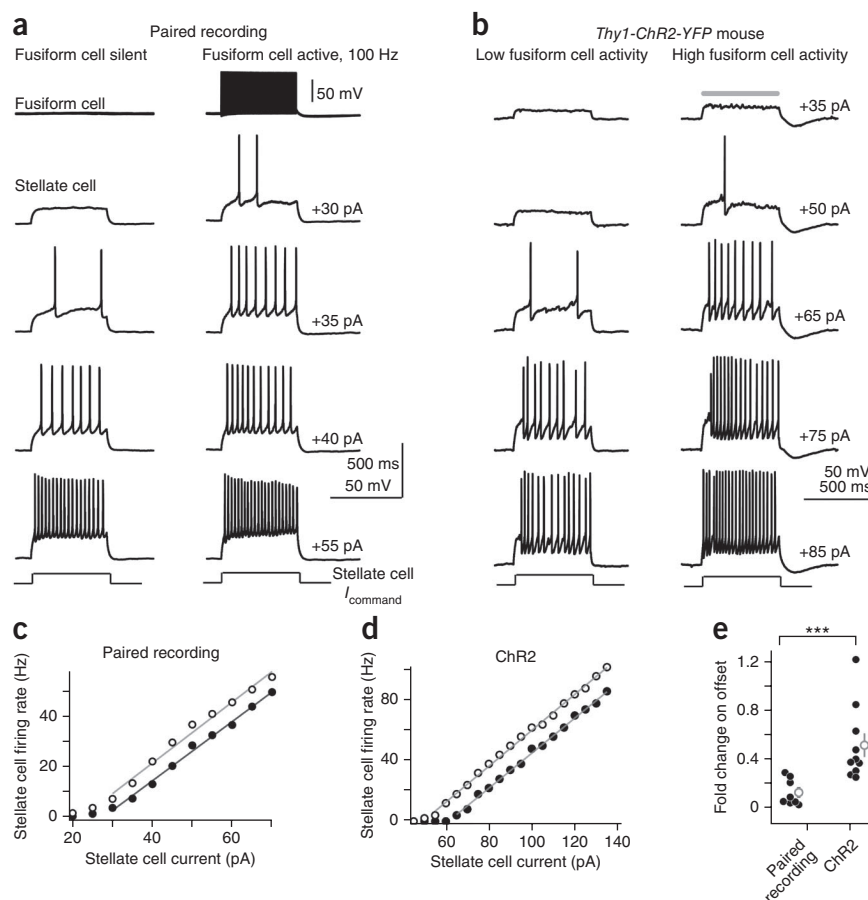
and stimulating the auditory nerve with a bipolar electrode placed in the ventral cochlear nucleus. In agreement with this possibility, trains of stimuli to the auditory nerve depolarized stellate cells (3.2 ± 0.5 mV; $n = 6$ cells; **Fig. 4d,e**). Two features of this response indicate that it occurred through gap junction coupling with fusiform cells. First, the depolarization was followed by a hyperpolarization (in current-clamp recordings) or an outward current (in voltage-clamp recordings; **Fig. 4d**), which is similar to the postjunctional activity that was generated by direct current injection in fusiform cells (**Fig. 4c**). The slow outward current seen in the voltage-clamp recordings likely reflects the membrane potential of prejunctional fusiform cells relaxing toward baseline during decay of the AHP. Second, depolarization of the stellate cell to 0 mV (recorded with a cesium-based internal solution), which markedly reduces the driving force for glutamatergic transmission, only mildly reduced the amplitude of the steady-state response (**Fig. 4e**; average amplitude at -67 mV, -17 ± 3 pA (mean \pm s.e.m.); 0 mV, -13 ± 3 pA; ratio of average current at 0 mV to -67 mV, 0.75 ± 0.03 ; $n = 5$ cells). Nevertheless, these voltage-independent responses were blocked entirely by bath application of AMPA and NMDA receptor blockers (10 μ M 6-nitro-2,3-dioxo-1,4-dihydro benzo[f]quinoxaline-7-sulfonamide (NBQX) and 5 μ M 3-((R)-2-carboxypiperazin-4-yl)-propyl-1-phosphonic acid (R-CPP), respectively), showing that they were generated by glutamatergic synaptic transmission (**Fig. 4e**; $n = 3$ cells). Thus, auditory nerve synapses generate excitatory responses that do not arise from transmitter-gated channels in stellate cells. These results strongly suggest that the auditory pathway transmits information to stellate cells, albeit independently of a direct auditory nerve projection into the molecular layer.

Optogenetic activation of multiple fusiform cells

Because auditory nerve input to the DCN is tonotopically organized, single fusiform cells respond best to a limited range of sound frequencies. If multiple prejunctional fusiform cells with similar frequency tunings converge on a single stellate cell, our paired recordings likely underestimate the extent to which electrical synapses may control stellate cell excitability. To determine the capacity of multiple prejunctional fusiform cells to control the stellate cell membrane potential, we performed experiments in transgenic mice expressing the light-activated cation channel channelrhodopsin2 (ChR2) driven by the *Thy1* promoter (*Thy1-ChR2-YFP* line 18 (ref. 26)) or the vesicular glutamate transporter 2 (*VGLUT2*, also called *Slc17a6*) promoter (*VGLUT2-ChR2-YFP*²⁷). Both lines robustly expressed ChR2 in fusiform cells: blue-light flashes delivered through the microscope objective caused large inward currents in voltage-clamped fusiform cells and reliably drove spiking in current-clamped cells (**Fig. 5a,d**). The absolute amplitudes of the photocurrents in voltage-clamped fusiform cells from *Thy1-ChR2-YFP* mice were on average significantly larger than those observed in the *VGLUT2-ChR2-YFP* line (*Thy1*, 991 ± 185 pA, $n = 19$ cells; *VGLUT2*, 225 ± 25 pA, $n = 13$ cells; $t(30) = 3.4$, $P = 0.002$, unpaired t test). However, we obtained similar results with the two lines for the optogenetic experiments shown in **Figures 5–7**, so we pooled the data (with mice from the two groups referred to hereafter generally as ChR2 mice).

In slices from ChR2 mice, blue light also robustly increased the firing frequency of stellate cells recorded in current clamp (**Fig. 5b,e**). We performed these experiments in the presence of NBQX and R-CPP, showing that the rapid increase in stellate cell spike rate was not due to ChR2 activation of presynaptic glutamatergic axons. We further investigated

Figure 6 Fusiform cells control the spike rate of stellate cells. **(a)** Single trials from an electrically coupled fusiform-stellate cell pair. The stellate cell was depolarized with step pulses of increasing positive current (2.5- to 5-pA intervals, 500-ms duration) in the absence or presence of simultaneous 100-Hz activity in the fusiform cell (left and right columns, respectively). Activity in the prejunctional fusiform cell increases the total number of spikes generated in the stellate cell with intermediate current steps. **(b)** Example single trials from a stellate cell in a *Thy1-ChR2-YFP* mouse. Traces show the stellate cell spikes evoked by positive current injection (500 ms) with (right) or without (left) concurrent blue-light flashes (gray bar; 500 ms) to activate prejunctional fusiform cells. **(c)** Input-output curve for the pair in **a**. The spike frequency (y axis) is plotted as a function of current injection. The solid points represent values while the prejunctional cell was silent, and the open points are values with concurrent prejunctional fusiform cell activity. The gray lines are linear fits to the nonzero portions of the data. **(d)** As in **c** but for the ChR2 experiment in **b**. The open and filled circles represent the input-output curves of the example cell in **b** with or without simultaneous blue-light flashes, respectively. **(e)** Summary graph plotting the normalized change in offset (x intercept) due to fusiform cell activity in the paired recordings and ChR2 experiments. Gray points are the mean \pm s.e.m. Asterisks denote statistical significance. Optogenetic stimulation caused a 3.7-fold greater shift in offset compared to paired recordings ($t(16) = 3.4$, $P = 0.004$, unpaired t test).



the depolarization underlying this phenomenon by hyperpolarizing stellate cells with a negative bias current to prevent spiking. As expected from activating prejunctional fusiform cells, blue light evoked trains of spikelets atop a steady depolarization (Fig. 5c,f) that, after light termination, were followed by the post-train AHP that was seen in the paired recordings (Fig. 4c). In voltage-clamped stellate cells, the same light stimuli caused biphasic 'postjunctional photocurrents' that were characterized by spikelets riding atop an inward current followed by a slow outward current after light termination (Fig. 5c,f). The amplitudes of the mean steady-state inward and peak outward postjunctional photocurrents were -16.9 ± 2.5 pA and 14.4 ± 1.8 pA, respectively ($n = 28$ cells). Careful inspection of the voltage-clamp traces revealed spikelets of different amplitudes (Fig. 5f,g), suggesting that multiple fusiform cells with different coupling coefficients contact a single stellate cell. Additionally, we never observed light-evoked spikelets, depolarizations or inward currents in cartwheel cells (0/37 cells tested), further highlighting the cell-type specificity of electrical coupling.

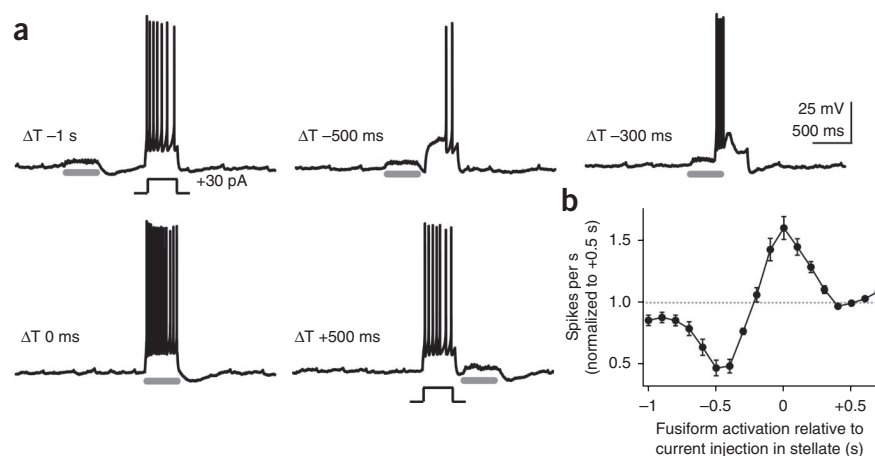
Several control experiments led us to reject the possibility that the light-evoked depolarizations and postjunctional photocurrents in stellate cells were due to direct ChR2 expression in the stellate cell plasma membrane. First, the *VGluT2-ChR2-YFP* line should show ChR2 expression that is restricted to excitatory glutamatergic neurons such as fusiform cells²⁸ and not in GABAergic stellate cells²⁹. Second, if postjunctional photocurrents are due to ChR2 expression in stellate cells, they should follow the current-voltage curve that has been documented in previous studies of the ChR2 cation channel and reverse at positive potentials³⁰. However, the postjunctional photocurrents in voltage-clamped stellate cells were only minimally voltage dependent and remained inward at +53 mV, as would be expected for a cation current arising through an

unclamped distal compartment (Supplementary Fig. 4a,b). By contrast, photocurrents in fusiform cells displayed a rectifying current-voltage relationship, which would be expected of the ChR2 channel and reversed at positive potentials. Third, the gap junction blocker MFA abolished postjunctional photocurrents in stellate cells but had little effect on ChR2 photocurrents in fusiform cells (Supplementary Fig. 4c,d). Together these data show that postjunctional photocurrents represent the summed activity of prejunctional fusiform cells and not ectopic expression of ChR2 in stellate cells. Bath application of tetrodotoxin (TTX; 500 nM) significantly reduced the amplitude of the stellate cell postjunctional depolarization by $38 \pm 4\%$ (baseline, 5.8 ± 1.0 mV; TTX, 3.4 ± 0.6 mV; $n = 14$; $t(13) = 4.6$, $P = 0.0005$, paired t test) and reduced the postjunctional AHP during the light-off response by $61 \pm 3\%$ (baseline, -5.2 ± 0.8 mV; TTX, -2.2 ± 0.5 mV; $n = 14$; $t(13) = 6.96$, $P < 0.0001$, paired t test). These data indicate that spikes in prejunctional fusiform cells contribute to the light-evoked depolarizations in stellate cells. Thus, active and passive depolarizations in fusiform cells are transmitted to stellate cells. Moreover, the fact that the ChR2-induced, TTX-sensitive depolarization (2.4 mV) in stellate cells was over twofold greater than the depolarization generated by stimulating a single fusiform cell (0.8 mV at 100 Hz) indicates that the ChR2-induced depolarization was indeed generated by multiple prejunctional fusiform cells.

Fusiform cells control stellate cell spike output

Can a single fusiform cell suffice to increase stellate cell spike output, or does this effect require simultaneous activity in multiple prejunctional cells? We recorded electrically coupled pairs and injected a family of depolarizing current steps into the stellate cell with or without simultaneous 100-Hz activity in the prejunctional

Figure 7 The timing of fusiform cell activity bidirectionally controls stellate cell spike output. (a) Single trials from a stellate cell in a *VGluT2-ChR2-YFP* mouse in which the cell was transiently driven to spike with injection of positive current (400 ms). Prejunctional fusiform cells were activated by blue light (gray bars; 400 ms) at various times relative to the current step in the stellate cell. Negative bias current was used to prevent spontaneous firing. (b) Summary graph from 13 stellate cells in ChR2 mice plotting normalized spikes per s as a function of flash timing relative to the stellate cell current injection. The data (means \pm s.e.m.) are normalized to the +500 ms data point, where the light flash (and thus, fusiform cell activation) occurred after the current step in the stellate cell.

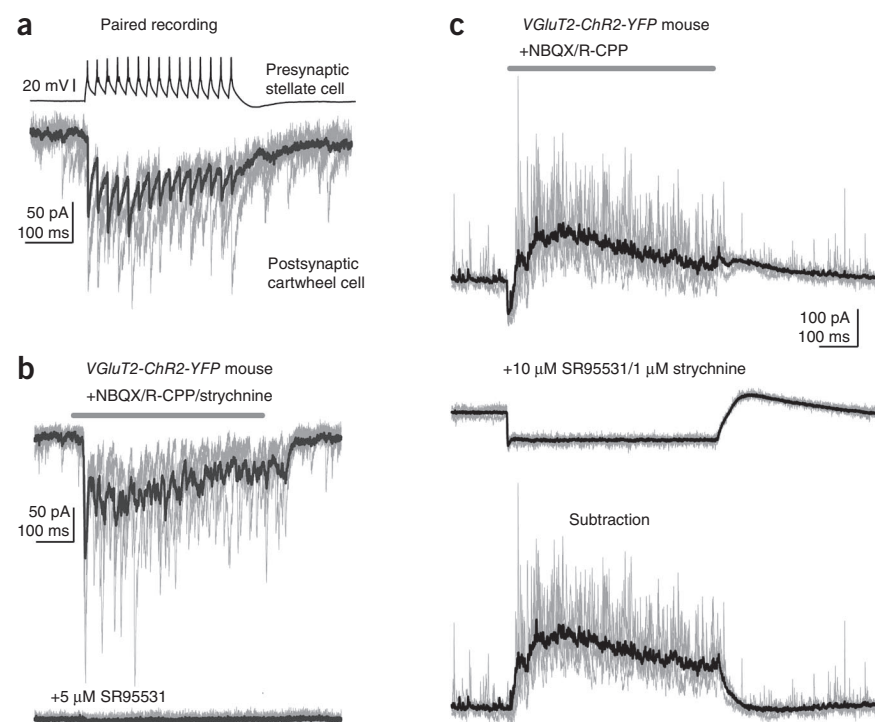


fusiform cell (Fig. 6a). We used negative bias current to prevent spontaneous firing of both neurons. We made a linear fit to the nonzero portions of the stellate cell input-output curves to compare the slope and offset (x intercept for $y = 0$) of the function during the two conditions³¹. In eight pairs tested, fusiform cell activity shifted the offset of the stellate cell input-output curves from 28.8 ± 5.0 pA during baseline to 25.2 ± 5.0 pA when the fusiform cell was active (Fig. 6c; $-13 \pm 4\%$ difference; $t(7) = 3$, $P = 0.02$, paired t test). However, fusiform cell activity had no significant effect on the slope of the input-output curve (baseline, 1.1 ± 0.1 pA Hz⁻¹; with fusiform cell activity, 1.2 ± 0.1 pA Hz⁻¹; $+4.5 \pm 2.8\%$ change; $t(7) = 1.53$, $P = 0.14$, paired t test). Furthermore, activating multiple prejunctional fusiform cells with blue-light stimuli in ChR2 mice (Fig. 6b) caused significantly

larger shifts in the offset of the stellate cell input-output functions (Fig. 6d; from 34.1 ± 5.4 pA to 15.1 ± 4.9 pA; $-52 \pm 10\%$ difference; $n = 10$ cells; $t(9) = 3.66$, $P = 0.005$, paired t test), with no significant change in the slope (1.6 ± 0.15 pA Hz⁻¹ to 1.47 ± 0.11 pA Hz⁻¹; $-6.8 \pm 4.3\%$ change; $t(9) = 1.34$, $P = 0.21$, paired t test). Thus, activity in even a single fusiform cell significantly enhances the excitability of local interneurons, and this represents a largely additive transformation of the stellate cell's input-output function.

The large postjunctional AHP observed in stellate cells after fusiform cell or auditory nerve spike trains (Figs. 4 and 5) suggests that the timing of fusiform cell activity determines whether electrical synapses exert a net excitatory or a net inhibitory effect on stellate cell spike output. We tested this idea by recording single stellate

Figure 8 Fusiform cells generate inhibition in the DCN. (a) Paired recording between a presynaptic stellate and postsynaptic cartwheel cell. GABAergic transmission was isolated with glutamate and glycine receptor blockers. Fifteen action potentials were elicited at 50 Hz in the stellate cell, resulting in a time-locked series of IPSCs in the postsynaptic cartwheel cell. IPSCs are inward as the cartwheel cell is recorded with a Cl⁻-rich internal solution. Gray traces represent four single sweeps, and the black trace shows an average of 20 trials. (b) A cartwheel cell in a *VGluT2-ChR2-YFP* mouse. Top trace, optogenetic stimulation of fusiform cells, denoted by the horizontal gray line, results in a barrage of IPSCs in the cartwheel cell. Lower trace, the GABA_A receptor antagonist SR95531 blocks the optogenetically evoked IPSCs. Gray traces represent four single sweeps, and the black trace is an average of ten trials in each condition. (c) Example recording from a fusiform cell in a *VGluT2-ChR2-YFP* mouse. The cell is voltage clamped at 0 mV, generating a net outward driving for Cl⁻ currents. Top, activating neighboring fusiform cells using blue-light stimuli (500 ms; horizontal gray line) causes a powerful increase in IPSC frequency. Middle, IPSCs are blocked by the addition of the GABA_A and glycine receptor blockers SR95531 and strychnine, revealing an inward photocurrent during the light stimulus. Gray traces represent five consecutive trials, and black traces are an average of 20–23 trials. Bottom, same example traces as those in the top recording but with the average photocurrent digitally subtracted. Thus, activation of neighboring fusiform cells causes an inhibitory outward current for the duration of the light stimulus.



cells in ChR2 mice and varying the time interval between depolarizing current steps in the stellate cell and blue-light stimuli, thereby allowing either the depolarizing or AHP phase of the fusiform cell activity to overlap with stellate cell spiking (Fig. 7a). The results were marked, as coincident activation of fusiform cells within a ± 100 -ms time window of stellate cell depolarization increased spike output by $50 \pm 5\%$ compared to baseline (Fig. 7b; $n = 13$). By contrast, activating fusiform cells 500 ms before stellate cell current injection, which resulted in maximal overlap of the postjunctional AHP and stellate cell depolarization, reduced the total number of spikes by $53 \pm 6\%$. Thus, the timing of fusiform cell activity with respect to stellate cell excitation bidirectionally regulates the number of spikes generated by the interneuron over a threefold range.

Fusiform cell activity generates local inhibition

Our data show that activity of even a single prejunctional fusiform cell is sufficient to excite stellate cells and thus predict that fusiform cell spiking should increase inhibition in the DCN molecular layer by depolarizing the stellate cell network. By homology to their cerebellar counterparts, stellate cells have been suggested to synapse onto the Purkinje-like cartwheel cells of the DCN^{12,32}. Accordingly, paired recordings revealed unitary stellate to cartwheel cell inhibitory postsynaptic currents (IPSCs) in 8/26 attempted pairs (30.8% connection probability; Fig. 8a).

To explicitly test whether fusiform cell activity generates inhibition in the DCN, we recorded from single cartwheel cells and optogenetically activated fusiform cells (300- to 500-ms light stimuli). In the majority of voltage-clamped cartwheel cells (25/28), optogenetic activation of fusiform cells triggered barrages of IPSCs (Fig. 8b) that were blocked entirely by the GABA_A receptor antagonist SR95531 (5 μ M; $n = 8$; Fig. 8b). These IPSCs were not due to polysynaptic recruitment of interneurons through glutamatergic synapses because excitatory transmission was blocked by 10 μ M NBQX and 5 μ M R-CPP in all experiments.

We also examined whether activation of fusiform cells could lead to inhibition of other fusiform cells through stellate to fusiform cell chemical synapses. We recorded voltage-clamped fusiform cells from *VGluT2-ChR2-YFP* mice near the reversal potential for the ChR2 photocurrent (0–13 mV) using a cesium-based internal solution. In 7 of 11 cells tested, blue-light stimuli generated barrages of IPSCs that were partially occluded by the small inward photocurrent (Fig. 8c). These IPSCs were not triggered by excitatory glutamatergic synapses because we performed all experiments in the presence of NBQX and R-CPP. Bath application of inhibitory synaptic blockers (SR95531 and strychnine; $n = 6$ cells) blocked the IPSCs, and subsequent digital subtraction of the average photocurrent trace from the single traces recorded in NBQX and R-CPP clearly showed that activation of neighboring fusiform cells generated a robust inhibitory response in the voltage-clamped neuron (Fig. 8c). Thus, principal neuron activity generates time-locked increases in local inhibition, thereby regulating the excitability of neighboring principal neurons and interneurons.

DISCUSSION

A hallmark of sensory circuits is that external stimuli recruit inhibition proportional to the magnitude of the excitatory drive³³. Whether the sensitivity of inhibitory neurons is fixed or labile with respect to a given stimulus is unclear. We have demonstrated a simple cellular mechanism that uses gap junctions to rapidly control the moment-to-moment dynamics of inhibition on the basis of the timing of principal neuron activity. The probability of electrical coupling between principal cells and interneurons was high (57%), suggesting that this transmission pathway constitutes a major component of the DCN circuit. Moreover, electrical coupling was robust in animals as old as

postnatal month 2, indicating that this circuit motif should function as a component of sensory processing and is not a transient developmental phenomenon. Thus, our findings raise the possibility that even at the earliest stages of auditory processing, ongoing sensory input bidirectionally regulates the threshold for recruiting local inhibition.

These results substantially revise the canonical DCN model in which multisensory and auditory inputs recruit distinct classes of interneurons⁴. Through electrical coupling with fusiform cells, the stellate cell membrane potential will rapidly sense ongoing auditory activity, a prediction that is supported by our observation that auditory nerve activation itself generates signals in stellate cells through gap junction coupling. There are no reports of recordings from identified stellate cells *in vivo*, presumably because of their small size and precarious location at the ependymal edge of the brainstem. Given that single stellate cells are coupled to multiple fusiform cells, our data suggest that electrical coupling may endow stellate cells with complex ‘best-frequency’ characteristics that reflect the additive frequency-tuning properties of prejunctional fusiform cells. Nevertheless, an understanding of how electrical coupling regulates information flow through the DCN will require knowing the functional connectivity between a stellate cell’s postsynaptic targets and its electrically coupled partners. Stellate cells form inhibitory synapses onto cartwheel and fusiform cells^{32,34} (Fig. 8). Activating stellate cells through the gap junction pathway generated IPSCs in a functionally silent (for example, voltage-clamped) fusiform cell (Fig. 8c,d), showing that stellate cells do not perform feedback inhibition strictly onto activated principal neurons. However, it is unknown whether stellate cells inhibit fusiform cells that are tuned to similar frequencies as those with which they form electrical synapses or whether they inhibit fusiform cells across frequencies (i.e., lateral inhibition). Similarly, the spatial distribution of cartwheel cell axons is not yet known, and it remains to be determined whether stellate cells inhibit cartwheel cells that control local or more distant fusiform cells.

Further studies will be required to definitively assign a specific functional role for the new circuit we identified. The DCN is organized similarly to the cerebellum and cerebellum-like structures that are found in mammals and weakly electric fish: fusiform cells are analogous to deep cerebellar nucleus neurons and the glutamatergic efferent cells of the mormyrid electric fish’s electrosensory lobe, whereas cartwheel cells are thought to function as the Purkinje-like cells of these circuits^{1,4}. Given that cerebellum-like circuits may mediate the adaptive filtering of self-generated sensory input, the molecular-layer circuitry of the DCN could facilitate a comparison of acoustic signals in the environment with body orientation or activity^{3,4}. A key cellular phenomenon that has been suggested to underlie such adaptive filtering is that coincident activity of predictive parallel fiber and instructive sensory pathways induces an anti-Hebbian, long-term depression of the active parallel fiber synapses^{35,36}. In the electrosensory lobe of the mormyrid electric fish, the Purkinje-like medium ganglion cells and excitatory efferent neurons integrate sensory information from electroreceptors on the skin (for example, instructive signals) with parallel fiber synapses that convey predictive information regarding the fish’s motor movements and behavior^{1,3}. Simultaneous pairing of motor commands with electrosensory signals leads to long-term depression of the active parallel fibers in Purkinje-like cells and efferent neurons^{37,38}. On a circuit level, this phenomenon is thought to be involved in generating activity patterns that are ‘negative images’ of predictable sensory input^{1,3}. However, experiments have shown that associative, long-term plasticity in cerebellum-like circuits requires prolonged induction protocols and is fully expressed only several minutes after induction^{17,36,38,39}. Our work suggests an alternative mechanism that might contribute to a moment-to-moment

reduction of parallel fiber synapses, thereby mediating adaptation to a rapidly changing environment. We found that activation of fusiform cells through the auditory pathway depolarizes stellate cells (Fig. 4d) and can thus sensitize molecular-layer interneurons to subthreshold parallel fiber inputs. Furthermore, fusiform cell activity alone is sufficient to generate robust inhibition onto two major targets of parallel fibers: cartwheel cells and neighboring fusiform cells (Fig. 8). Thus, auditory signals could, in principle, rapidly recruit or suppress stellate cells and control the efficacy of parallel fiber activity, depending on the relative timing of auditory and nonauditory sensory signals. Interestingly, recent studies have suggested that cerebellar stellate cells sense glutamate ‘spillover’ from climbing fiber synapses^{40–42} and that feedforward inhibition generated by climbing fiber activity is sufficient to rapidly decrease the capacity of parallel fibers to drive spikes in neighboring Purkinje cells⁴². Together with our data, these findings imply that transmission of instructive signals to molecular-layer interneurons may be a general feature of cerebellum-like circuits.

METHODS

Methods and any associated references are available in the [online version of the paper](#).

Note: Any Supplementary Information and Source Data files are available in the online version of the paper.

ACKNOWLEDGMENTS

We thank M. Roberts and S. Kuo for preliminary observations that led us to search for electrical coupling in the DCN; M. Bateschell and R. Larisch for help with mouse colony management and genotyping; C. Borges-Merjane (Vollum Institute/Oregon Hearing Research Center) for initially genotyping the *Thy1-ChR2* mice and providing the cerebellum slices used in [Supplementary Figure 2](#); H.-W. Lu for writing the macros used to analyze the calcium imaging data; S. Foster for performing the auditory brainstem response measurements; and K. Bender, W. Giardino and N. Sawtell for critical comments on the manuscript. Funding was provided by US National Institutes of Health grants R01DC004450 to L.O.T., F31DC012222 to P.F.A. and P30 DC005983 to the Oregon Hearing Research Center.

AUTHOR CONTRIBUTIONS

P.F.A. collected the data. P.F.A. and L.O.T. designed the study, analyzed and interpreted the results and wrote the manuscript.

COMPETING FINANCIAL INTERESTS

The authors declare no competing financial interests.

Reprints and permissions information is available online at <http://www.nature.com/reprints/index.html>.

- Bell, C.C., Han, V. & Sawtell, N.B. Cerebellum-like structures and their implications for cerebellar function. *Annu. Rev. Neurosci.* **31**, 1–24 (2008).
- Dean, P., Porrill, J., Ekerot, C.-F. & Jörntell, H. The cerebellar microcircuit as an adaptive filter: experimental and computational evidence. *Nat. Rev. Neurosci.* **11**, 30–43 (2010).
- Requarth, T. & Sawtell, N.B. Neural mechanisms for filtering self-generated sensory signals in cerebellum-like circuits. *Curr. Opin. Neurobiol.* **21**, 602–608 (2011).
- Oertel, D. & Young, E.D. What's a cerebellar circuit doing in the auditory system? *Trends Neurosci.* **27**, 104–110 (2004).
- Roberts, M.T. & Trussell, L.O. Molecular layer inhibitory interneurons provide feedforward and lateral inhibition in the dorsal cochlear nucleus. *J. Neurophysiol.* **104**, 2462–2473 (2010).
- Bennett, M.V.L. & Zukin, R.S. Electrical coupling and neuronal synchronization in the mammalian brain. *Neuron* **41**, 495–511 (2004).
- Hestrin, S. & Galarreta, M. Electrical synapses define networks of neocortical GABAergic neurons. *Trends Neurosci.* **28**, 304–309 (2005).
- Christie, M.J., Williams, J.T. & North, R.A. Electrical coupling synchronizes subthreshold activity in locus coeruleus neurons *in vitro* from neonatal rats. *J. Neurosci.* **9**, 3584–3589 (1989).
- Maher, B.J., McGinley, M.J. & Westbrook, G.L. Experience-dependent maturation of the glomerular microcircuit. *Proc. Natl. Acad. Sci. USA* **106**, 16865–16870 (2009).
- Bennett, M.V. Physiology of electrotonic junctions. *Ann. NY Acad. Sci.* **137**, 509–539 (1966).
- Gibson, J.R., Beierlein, M. & Connors, B.W. Two networks of electrically coupled inhibitory neurons in neocortex. *Nature* **402**, 75–79 (1999).
- Wouterlood, F.G., Mugnaini, E., Osen, K.K. & Dahl, A.L. Stellate neurons in rat dorsal cochlear nucleus studies with combined Golgi impregnation and electron microscopy: synaptic connections and mutual coupling by gap junctions. *J. Neurocytol.* **13**, 639–664 (1984).
- Mann-Metzer, P. & Yarom, Y. Electrotonic coupling interacts with intrinsic properties to generate synchronized activity in cerebellar networks of inhibitory interneurons. *J. Neurosci.* **19**, 3298–3306 (1999).
- Leao, R.M., Li, S., Doiron, B. & Tzounopoulos, T. Diverse levels of an inwardly rectifying potassium conductance generate heterogeneous neuronal behavior in a population of dorsal cochlear nucleus pyramidal neurons. *J. Neurophysiol.* **107**, 3008–3019 (2012).
- Davis, K.A. & Young, E.D. Pharmacological evidence of inhibitory and disinhibitory neuronal circuits in dorsal cochlear nucleus. *J. Neurophysiol.* **83**, 926–940 (2000).
- Molitor, S.C. & Manis, P.B. Dendritic Ca^{2+} transients evoked by action potentials in rat dorsal cochlear nucleus pyramidal and cartwheel neurons. *J. Neurophysiol.* **89**, 2225–2237 (2003).
- Tzounopoulos, T., Kim, Y., Oertel, D. & Trussell, L.O. Cell-specific, spike timing-dependent plasticities in the dorsal cochlear nucleus. *Nat. Neurosci.* **7**, 719–725 (2004).
- Zhang, S. & Oertel, D. Neuronal circuits associated with the output of the dorsal cochlear nucleus through fusiform cells. *J. Neurophysiol.* **71**, 914–930 (1994).
- Dugué, G.P. *et al.* Electrical coupling mediates tunable low-frequency oscillations and resonance in the cerebellar Golgi cell network. *Neuron* **61**, 126–139 (2009).
- Vervaeke, K. *et al.* Rapid desynchronization of an electrically coupled interneuron network with sparse excitatory synaptic input. *Neuron* **67**, 435–451 (2010).
- Gibson, J.R., Beierlein, M. & Connors, B.W. Functional properties of electrical synapses between inhibitory interneurons of neocortical layer 4. *J. Neurophysiol.* **93**, 467–480 (2005).
- Ma, W.-L.D. & Brenowitz, S.D. Single-neuron recordings from unanesthetized mouse dorsal cochlear nucleus. *J. Neurophysiol.* **107**, 824–835 (2012).
- Rhode, W.S., Smith, P.H. & Oertel, D. Physiological response properties of cells labeled intracellularly with horseradish peroxidase in cat dorsal cochlear nucleus. *J. Comp. Neurol.* **213**, 426–447 (1983).
- Hancock, K.E. & Voigt, H.F. Intracellularly labeled fusiform cells in dorsal cochlear nucleus of the gerbil. I. Physiological response properties. *J. Neurophysiol.* **87**, 2505–2519 (2002).
- Merchan, M.A., Collia, F.P., Merchan, J.A. & Saldana, E. Distribution of primary afferent fibres in the cochlear nuclei. A silver and horseradish peroxidase (HRP) study. *J. Anat.* **141**, 121–130 (1985).
- Arenkiel, B.R. *et al.* *In vivo* light-induced activation of neural circuitry in transgenic mice expressing channelrhodopsin-2. *Neuron* **54**, 205–218 (2007).
- Hägglund, M., Borgius, L., Dougherty, K.J. & Kiehn, O. Activation of groups of excitatory neurons in the mammalian spinal cord or hindbrain evokes locomotion. *Nat. Neurosci.* **13**, 246–252 (2010).
- Ito, T. & Oliver, D.L. Origins of glutamatergic terminals in the inferior colliculus identified by retrograde transport and expression of VGLUT1 and VGLUT2 genes. *Front. Neuroanat.* **4**, 135 (2010).
- Mugnaini, E. GABA neurons in the superficial layers of the rat dorsal cochlear nucleus: light and electron microscopic immunocytochemistry. *J. Comp. Neurol.* **235**, 61–81 (1985).
- Nagel, G. *et al.* Channelrhodopsin-2, a directly light-gated cation-selective membrane channel. *Proc. Natl. Acad. Sci. USA* **100**, 13940–13945 (2003).
- Mitchell, S.J. & Silver, R.A. Shunting inhibition modulates neuronal gain during synaptic excitation. *Neuron* **38**, 433–445 (2003).
- Rubio, M.E. & Juiz, J.M. Differential distribution of synaptic endings containing glutamate, glycine, and GABA in the rat dorsal cochlear nucleus. *J. Comp. Neurol.* **477**, 253–272 (2004); erratum 485, 266 (2005).
- Isaacson, J.S. & Scanziani, M. How inhibition shapes cortical activity. *Neuron* **72**, 231–243 (2011).
- Osen, K.K., Ottersen, O.P. & Storm-Mathisen, J. Colocalization of glycine-like and GABA-like immunoreactivities: a semi-quantitative study of individual neurons in the dorsal cochlear nucleus of cat. In *Glycine Neurotransmission* (eds. Ottersen, O.P. & Storm-Mathisen, J.): 417–451 (J. Wiley and Sons, New York, 1990).
- Bell, C.C., Han, V.Z., Sugawara, Y. & Grant, K. Synaptic plasticity in a cerebellum-like structure depends on temporal order. *Nature* **387**, 278–281 (1997).
- Han, V.Z., Grant, K. & Bell, C.C. Reversible associative depression and nonassociative potentiation at a parallel fiber synapse. *Neuron* **27**, 611–622 (2000).
- Bell, C.C., Caputi, A. & Grant, K. Physiology and plasticity of morphologically identified cells in the mormyrid electrosensory lobe. *J. Neurosci.* **17**, 6409–6423 (1997).
- Sawtell, N.B. & Williams, A. Transformations of electrosensory encoding associated with an adaptive filter. *J. Neurosci.* **28**, 1598–1612 (2008).
- Hansel, C. *et al.* $CaMKII$ is essential for cerebellar LTD and motor learning. *Neuron* **51**, 835–843 (2006).
- Szapiro, G. & Barbour, B. Multiple climbing fibers signal to molecular layer interneurons exclusively via glutamate spillover. *Nat. Neurosci.* **10**, 735–742 (2007).
- Mathews, P.J., Lee, K.H., Peng, Z., Houser, C.R. & Otis, T.S. Effects of climbing fiber driven inhibition on Purkinje neuron spiking. *J. Neurosci.* **32**, 17988–17997 (2012).
- Coddington, L.T., Rudolph, S., Vande Lune, P., Overstreet-Wadiche, L. & Wadiche, J.I. Spillover-mediated feedforward inhibition functionally segregates interneuron activity. *Neuron* **78**, 1050–1062 (2013).

ONLINE METHODS

DCN brain slice preparation. All procedures involving animals were approved by Oregon Health and Science University's Institutional Animal Care and Use Committee. C57BL/6 wild-type mice of either sex at postnatal day 15–32 were used for the majority of the experiments. For optogenetic experiments, the mice were B6.Cg-Tg(*Thy1-COP4/eYFP*)18Gfng/J (*Thy1-ChR2-YFP*; JAX stock # 007612) or C57BL/6-Tg(*Slc17a6-COP4*H134R/eYFP*)20Ki/J (*VGluT2-ChR2-YFP*; JAX stock # 017978). Mice were anesthetized by isoflurane inhalation and then decapitated, and 200- to 250- μ m coronal DCN slices were cut in a cold sucrose solution containing (in mM) 87 NaCl, 25 NaHCO₃, 25 glucose, 7.5 sucrose, 2.5 KCl, 1.25 NaH₂PO₄, 0.5 CaCl₂ and 7 MgCl₂ and bubbled with 5% CO₂ and 95% O₂. After cutting, slices were allowed to recover for 30–45 min at 34 °C in an artificial cerebrospinal fluid (ACSF) solution containing (in mM) 130 NaCl, 2.1 KCl, 1.7 CaCl₂, 1 MgSO₄, 1.2 KH₂PO₄, 20 NaHCO₃, 3 Na–4-(2-hydroxyethyl)-1-piperazineethanesulfonic acid (HEPES) and 10–12 glucose bubbled with 5% CO₂ and 95% O₂ (300–310 mOsm). In some experiments, 5 μ M R-CPP, 50 μ M D(-)-2-amino-5-phosphonovaleric acid (AP5) or 5 μ M MK801 was added to the slice and recovery solutions. After recovery, slices were kept at room temperature (~22 °C) until recording.

For DCN slices from mature animals, postnatal day (P) 54–63 mice were anesthetized with an intraperitoneal injection of 2% Avertin and transcardially perfused, and the brain was sliced in a chilled solution containing (in mM) 93 N-methyl-D-glucamine (NMDG), 2.5 KCl, 1.2 NaH₂PO₄, 30 NaHCO₃, 20 HEPES, 10 MgSO₄, 0.5 ascorbic acid, 2 thiourea, 3 Na-pyruvate, 25 glucose, 0.5 CaCl₂, 0.005 MK801 and 12 N-acetyl-L-cysteine, 300–310 mOsm, pH adjusted to 7.3–7.4 with HCl⁴³. Slices recovered at 34 °C in an NMDG-based solution for 10–15 min followed by a 40–60 min recovery period at room temperature in standard ACSF.

Electrophysiology. Slices were transferred to a recording chamber and continuously perfused at 3–4 ml per min with ACSF heated to 32–34 °C by an inline heater. Neurons were visualized by Dodt contrast optics with a 40 \times objective. Chemical synaptic transmission was blocked in most of the experiments shown in **Figures 1–3** and **5–7** by adding (in μ M) 10 NBQX, 5 R-CPP (or 50 AP5 or 5 MK801), 0.5–2 strychnine and 5–10 SR95531. 0.5–1 μ M TTX was sometimes added to the experiments shown in **Figure 1** and **Supplementary Figures 3** and **4** to stop spontaneous firing. For the experiments shown in **Figure 4d,e**, NBQX and R-CPP were omitted to enable the activation of auditory nerve synapses. Fusiform cells were identified by previously published criteria^{5,44}. Superficial stellate cells were identified by their location at the ependymal edge of the DCN molecular layer and soma size¹². Stellate cells could be easily distinguished from cartwheel cells by their smaller soma located at the ependymal edge of the DCN, stronger membrane potential sag upon hyperpolarization and significantly higher input resistances (stellate, 996 ± 139 M Ω , $n = 29$; cartwheel, 50 ± 4 M Ω , $n = 12$; $t(39) = 4.2937$, $P = 0.0001$, unpaired t test). In addition, 30 μ M Alexa488 (or 20 μ M Alexa594) was added to the pipette solution in many experiments to visualize the somatodendritic morphology. The pipette solution for most current- and voltage-clamp experiments contained (in mM) 113 K-gluconate, 4.8 MgCl₂, 4 ATP, 0.5 Tris-GTP, 14 Tris-phosphocreatine, 0.1 ethylene glycol tetraacetic acid (EGTA) and 10 HEPES, pH 7.25 with KOH, ~290 mOsm. In some of the experiments shown in **Figure 1**, 15.5 mM KCl was substituted for equimolar K-gluconate. For the current-voltage curves shown in **Supplementary Figure 4**, the internal solution contained (in mM) 64.5 CsMeSO₃, 30 CsF, 5 tetraethylammonium (TEA)-Cl, 5 QX314-Cl, 5 Cs₄-1,2-bis-(*o*-aminophenoxy)-ethane-*N,N,N',N',N''*,2-tetraacetic acid (BAPTA), 4.8 MgCl₂, 4 ATP, 0.5 GTP, 10 Tris-phosphocreatine and 10 HEPES. In some experiments, CsF was replaced with 15 mM CsMeSO₃ and 15.5 mM CsCl. Data are corrected for experimentally determined liquid junction potentials of 7 or 10 mV (for the CsMeSO₃ and K-gluconate internal solutions, respectively). For the paired recordings shown in **Figure 8**, 10 mM GABA was added to the presynaptic K-gluconate solution to reduce transmitter washout during whole-cell dialysis⁴⁵, and the cartwheel cells shown in **Figure 8a,b** were recorded with a cesium-based internal solution containing 103 mM CsCl in place of CsMeSO₃ and CsF. The fusiform cells shown in **Figure 8c,d** were recorded with the CsMeSO₃ internal solution. Pipette resistances for fusiform or cartwheel and stellate cells were typically 2–3 and 3–5 M Ω , respectively. In current-clamp recordings, the pipette capacitance was canceled, and the bridge balance was maintained. For voltage-clamp recordings, neurons were held between –60 and –80 mV. Series resistance (<15 and 25 M Ω for fusiform or cartwheel

and stellate cells, respectively) was compensated with a 60–80% ‘correction’ and a 90% ‘prediction’ (bandwidth, 3 kHz), and experiments were discarded if the series resistance varied more than 20–25%. Stimulation of auditory nerve fibers (50- to 100- μ s pulses, 0.5–5 V) was performed using a bipolar metal electrode positioned in the VCN in a coronal slice that contained both cochlear nuclear divisions. Optogenetic stimulation was performed as described in ref. 45 or using a custom-built, transistor-transistor logic-gated blue light-emitting diode light source.

Two-photon imaging. The two-photon imaging system (Prairie Technologies) is described in detail in ref. 46. For Ca²⁺ imaging experiments, EGTA in the K-gluconate internal solution was replaced with 150–200 μ M Fluo-5F and 20 μ M Alexa594. A Ti:sapphire pulsed laser (Coherent Chameleon Ultra II) was set to 810 nm, and line scans (2–2.4 ms) were performed at multiple sites along the somatodendritic axis of fusiform cells. Epifluorescence and transfluorescence signals were collected with a 40 \times , 0.8 numerical aperture (NA) objective and a 1.4 NA oil immersion condenser. For imaging the morphology of coupled pairs, the laser was set to 800 nm; stellate and fusiform cells were filled with 20–30 μ M Alexa594 or 90 μ M Alexa488, respectively.

Auditory brainstem response. For assurance that the *Gjd2*^{–/–} knockout mice did not have gross abnormalities in auditory function, we measured auditory brainstem responses. Three knockout and three wild-type mice (P30–P33) were anesthetized with a ketamine and xylazine cocktail, their eyes were coated with Altalube (15% mineral oil and 85% white petroleum) to prevent drying, and the mice were then placed on a heating pad in a sound-proof chamber. The experimenter was blinded to the genotype of the animals. Needle electrodes were placed subcutaneously near the ear at the vertex, with reference electrodes placed at the level of the scalp and thorax. Each ear was then stimulated separately with a closed tube sound delivery system sealed into the ear canal. The auditory brainstem response to a 1-ms rise-time tone burst at 4, 8, 12, 16, 24 and 32 kHz was recorded, and thresholds for visually obvious peak 1 and 4 responses were obtained for each ear. The average thresholds were identical for wild-type and knockout mice across all tested frequencies ($F(1,24) = 0.0005$, $P = 0.99$, two-way analysis of variance (ANOVA)).

Data acquisition and analysis. Electrophysiology data were recorded using Pclamp 9 software with a Molecular Devices Multiclamp 700B amplifier and a Digidata 1332A analog-to-digital converter board. Signals were acquired at 20–50 kHz and low-pass filtered at 1–10 kHz for offline analysis. Ca²⁺ imaging experiments were analyzed using custom macros in ImageJ or Igor; data are expressed as the ratio of the change in green signal divided by the background red signal ($\Delta G/R$) \times 100, and each trace is an average of 20–25 events. Ca²⁺ transient amplitudes were calculated by extrapolating the peak from monoexponential fits to the fluorescence decay at the end of the action potential train.

Coupling conductances between cells were calculated according to equation 7 of ref. 10, which is based on current responses and estimates of input resistance. Although the results suggested directional rectification of gap junction conductance between fusiform and stellate cells, the high input resistance of stellate cells makes it difficult to estimate an input resistance independently of junctional resistances in the network. The equation also does not account for dendritic cable properties. These issues may account for the seemingly lower junctional conductance in the fusiform to stellate direction despite the higher coupling coefficient as compared to the stellate to fusiform direction. In any case, it is likely that the tenfold higher resistance of stellate cells is the dominant factor in the greater efficacy of transmission from fusiform to stellate cells. Similar results were obtained using the equations of ref. 47.

Statistics. Data were analyzed with the statistical tests listed in the main text. For ANOVA, α was corrected for multiple comparisons, and individual comparisons were made using Dunnett's multiple comparisons test. χ^2 tests were performed with Yates's correction. All errors shown are the s.e.m.

Reagents. NBQX, R-CPP, AP5, TTX and SR95531 were from Abcam. Strychnine, MK801 and MFA were from Sigma-Aldrich.

43. Zhao, S. *et al.* Cell type-specific channelrhodopsin-2 transgenic mice for optogenetic dissection of neural circuitry function. *Nat. Methods* **8**, 745–752 (2011).

44. Kuo, S.P. & Trussell, L.O. Spontaneous spiking and synaptic depression underlie noradrenergic control of feed-forward inhibition. *Neuron* **71**, 306–318 (2011).
45. Apostolides, P.F. & Trussell, L.O. Rapid, Activity-independent turnover of vesicular transmitter content at a mixed glycine/GABA synapse. *J. Neurosci.* **33**, 4768–4781 (2013).
46. Bender, K.J., Ford, C.P. & Trussell, L.O. Dopaminergic modulation of axon initial segment calcium channels regulates action potential initiation. *Neuron* **68**, 500–511 (2010).
47. Devor, A. & Yarom, Y. Electrotonic coupling in the inferior olivary nucleus revealed by simultaneous double patch recordings. *J. Neurophysiol.* **87**, 3048–3058 (2002).